The Astrophysical Journal, 1002:25 (14pp), 2026 May 1 https://doi.org/10.3847/1538-4357/ae548d

The Emergence of Little Red Dots from Binary Massive Black Holes

Kohei Inayoshi[1], Jinyi Shangguan[1], Xian Chen[1,2], Luis C. Ho[1,2], and Zoltán Haiman[3,4,5]
[1] Kavli Institute for Astronomy and Astrophysics, Peking University, Beijing 100871, People's Republic of China; inayoshi@pku.edu.cn
[2] Department of Astronomy, School of Physics, Peking University, Beijing 100871, People's Republic of China
[3] Department of Astronomy, Columbia University, MC 5246, 538 West 120th Street, New York, NY 10027, USA
[4] Department of Physics, Columbia University, MC 5255, 538 West 120th Street, New York, NY 10027, USA
[5] Institute of Science and Technology Austria, AM Campus 1, Klosterneuburg 3400, Austria

Received 2025 May 15; revised 2026 January 15; accepted 2026 March 10; published 2026 April 22

Abstract

Little red dots (LRDs) are a newly identified class of broad-line active galactic nuclei (AGNs) with a distinctive V-shaped spectrum characterized by red optical and blue UV continuum emission. Their high abundance at redshifts of $z \sim 6$–8 and decline at lower redshifts suggest a transient origin. We propose that the spectral shape of LRDs originates from compact binary black hole systems, in which each black hole is surrounded by a mini-disk and embedded within a larger circumbinary disk. With a binary separation of $\lesssim 10^3$ Schwarzschild radii, the Wien tail of a $T \simeq 5000$ K blackbody spectrum at the inner edge of the circumbinary disk produces the red optical emission, while the mini-disks power the UV continuum. Binary torques carve out a gap between the circumbinary disk and the mini-disks, setting the turnover wavelength of the V-shaped spectrum around the Balmer limit. This scenario naturally reproduces LRD spectra requiring only modest dust attenuation ($A_V \lesssim 1$ mag), resolving overestimated luminosities for LRDs in previous studies and alleviating a tension with the so-called Sołtan argument. This model predicts distinct spectral evolution as the binary orbit decays through binary disk interactions and gravitational-wave (GW) emission, linking early-stage "proto-LRD" binaries to the broader AGN population and late-stage "LRD descendants" to coalescing binaries detectable in GW experiments.

Unified Astronomy Thesaurus concepts: Supermassive black holes (1663); Quasars (1319); High-redshift galaxies (734)

1. Introduction

Little red dots (LRDs) represent one of the most intriguing populations uncovered in recent James Webb Space Telescope (JWST) observations. They are considered a new class of broad-line active galactic nuclei (AGNs) powered by massive black holes (BHs) with masses of $M_{\rm BH} \simeq 10^{6-8} M_{\odot}$. Their spectral energy distribution (SED) is characterized by a distinctive V shape, with a red continuum in the rest-frame optical and a blue continuum in the rest-frame UV (D. D. Kocevski et al. 2023; G. Barro et al. 2024; J. Matthee et al. 2024; K. N. Hainline et al. 2025; I. Labbe et al. 2025), and a turnover wavelength near the Balmer limit (L. J. Furtak et al. 2023; J. E. Greene et al. 2024; B. Wang et al. 2024; D. J. Setton et al. 2025a).

The cosmic abundance of LRDs is ∼1–2 orders of magnitude higher than that of UV-bright quasars discovered by ground-based telescopes (e.g., L. Jiang et al. 2016; Y. Matsuoka et al. 2016; M. Niida et al. 2020; Y. Matsuoka et al. 2023), yet reaches ∼1% of the faint galaxy populations at similar redshifts (e.g., V. Kokorev et al. 2024a; X. Lin et al. 2024; H. B. Akins et al. 2025; D. D. Kocevski et al. 2025; X. Lin et al. 2026). If their bolometric luminosities estimated from SED fitting using dust-obscured AGN models are taken at face value, the inferred cosmic BH accretion rate density (BHAD) appears too high to be reconciled with a standard 10% radiative efficiency, suggesting that the BHs need to have substantially high spins (K. Inayoshi & K. Ichikawa 2024). Although rapidly spinning BHs are expected to launch jets via the Blandford–Znajek mechanism (R. D. Blandford & R. L. Znajek 1977), LRDs show no obvious (or only weak) X-ray and radio counterparts (M. Yue et al. 2024; A. J. Gloudemans et al. 2025; R. Maiolino et al. 2025; G. Mazzolari et al. 2026). This weak nonthermal radiation could be explained by radiative signatures of super-Eddington accreting BHs (P. Madau & F. Haardt 2024; F. Pacucci & R. Narayan 2024; K. Inayoshi et al. 2025). A possible resolution to this tension is that the intrinsic luminosities of LRDs have been overestimated due to uncertainties in dust-reddening corrections in the SED fitting process, as noted by K. Inayoshi & K. Ichikawa (2024). If this is the case, the inferred BHAD could be reconciled with a standard ∼10% radiative efficiency, alleviating the need for extreme BH spin and bringing the LRD population into agreement with the classical Sołtan–Paczyński argument (A. Soltan 1982; Q. Yu & S. Tremaine 2002).

Previous studies have attempted to explain the V-shaped SEDs using two-component models. These models attribute the UV emission to an unobscured galaxy or scattered AGN light, and the optical emission to an obscured galaxy or obscured AGN (D. D. Kocevski et al. 2023; B. Wang et al. 2024; Y. Ma et al. 2025), with a possible contribution from variations in dust attenuation laws in the UV (Z. Li et al. 2025b). However, all of these scenarios require fine-tuning of the relative contributions of each component to reproduce the observed SEDs, and the underlying physical origin of this balance remains unclear. Whether this ratio is coincidental or reflects a deeper physical process is still debated. The presence of a Balmer break in observed LRD spectra provides a crucial clue to stellar contributions from their host galaxies (V. Kokorev et al. 2024b; I. Labbe et al. 2024; B. Wang et al. 2024). However, in some

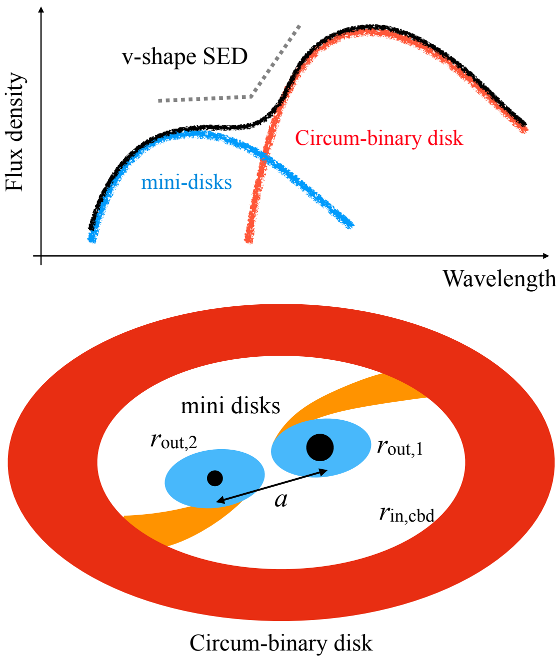

Figure 1. A schematic illustration of a binary BH system accreting from a circumbinary disk, with each BH surrounded by a mini-disk. The expected SED, composed of the cooler circumbinary disk and the hotter mini-disks, naturally produces a characteristic V shape, consistently observed in LRDs.

cases the Balmer break is too strong to be explained by stellar populations alone. Instead, it may result from dense neutral gas absorbers in which atomic hydrogen is excited to the $n = 2$ state, imprinting a Balmer break on the transmitted AGN spectrum (K. Inayoshi & R. Maiolino 2025; X. Ji et al. 2025).

Furthermore, the faint rest-frame near-IR (NIR) emission of LRDs suggests a lack of hot, dusty tori surrounding the AGNs (P. G. Pérez-González et al. 2024; B. Wang et al. 2024; C. C. Williams et al. 2024; H. B. Akins et al. 2025). This could be explained by clumpy or extended dusty media (C. M. Casey et al. 2024; Z. Li et al. 2025b) or simply by lower dust attenuation. An even more extreme possibility is that the red optical and faint NIR continuum emission can be well fitted by a blackbody spectrum with a photospheric temperature of $T_{\rm ph} \sim 5000\,{\rm K}$. This temperature corresponds to the lowest possible value for a (quasi-)hydrostatic object, set by $\rm H^-$ ions, and follows the so-called Hayashi line, observed as a vertical track on the Hertzsprung–Russell diagram (C. Hayashi 1961). Theoretically, such structures could be maintained as radiation-pressure-dominated envelopes surrounding rapidly accreting BHs at super-Eddington rates. Potential candidates include hyper-Eddington accretion flows (K. Inayoshi et al. 2016; E. Takeo et al. 2020; Y. Shi et al. 2023), quasi-stars (M. C. Begelman et al. 2006, 2008; M. Volonteri & M. C. Begelman 2010; E. R. Coughlin & M. C. Begelman 2024; D. Kido et al. 2025), or supermassive stars in a tentative stellar phase of direct-collapse BH formation (T. Hosokawa et al. 2013; T. E. Woods et al. 2021; L. Mayer et al. 2024). A recent study by R. P. Naidu et al. (2025) reported an LRD with an exceptionally strong Balmer break, possibly associated with a highly Compton-thick gas envelope around the AGN, which aligns with these theoretical models.

Beyond their spectral features, the cosmic evolution of LRDs offers further clues to their nature (D. D. Kocevski et al. 2025). Their abundance rises from $z \gtrsim 8$, peaks at $z \sim 6$, and declines sharply at $z \lesssim 4$. This transient-like appearance follows a log-normal distribution, suggesting that the AGN phase associated with LRDs is triggered by a distinctive early process and fades over time without recurring at later epochs (K. Inayoshi 2025). This declining trend is steeper than expected from galaxy (major) mergers alone, which would produce more extended systems and blur their distinctive characteristics. Alternatively, F. M. Khan et al. (2025) proposed that LRDs may transition into elliptical galaxies through mergers, and thus lose their defining characteristics. If galaxy mergers and subsequent BH coalescences contribute to the disappearance of LRDs, they would also produce gravitational-wave (GW) events at high redshifts (e.g., H. Liu & K. Inayoshi 2025) and the contribute to the stochastic GW background. A self-consistent theoretical model must therefore link this transient behavior to the physical origin of the V-shaped SEDs that characterize LRDs.

In this work, we propose an alternative explanation: the V-shaped SED of LRDs arises from a massive binary BH system, in which each BH is surrounded by a circum-BH disk (hereafter "mini-disk") and the system is embedded within a larger circumbinary disk. In this model, the mini-disks have higher effective temperatures, while the circumbinary disk has a lower effective temperature. With an appropriate binary separation of $\sim 10^3$ Schwarzschild radii (for the total mass of the BHs), the red optical continuum originates from the Wien tail of a blackbody spectrum with $T \sim 5000\,{\rm K}$ at the inner edge of the circumbinary disk, while the UV continuum is produced by emission from the mini-disks. Importantly, this model does not require strong dust attenuation, which is often assumed in SED fitting in the literature, but instead requires $A_V \lesssim 1$ mag to reproduce the spectral indices used in LRD selection.

This paper is organized as follows. In Section 2, we describe our spectral toy model for a binary BH embedded within a circumbinary disk with two mini-disks. In Section 3, we demonstrate how the SED model reproduces the spectral characteristics of LRDs, as well as the spectral evolution driven by binary orbital decay associated with binary disk interactions and GW emission. In Section 4, we discuss the implications of our model framework for the LRD abundance and the Sołtan argument, and we summarize our conclusions in Section 5.

2. Disk Spectral Model

We describe a spectral model for a binary BH system embedded within a circumbinary disk, with each BH surrounded by a mini-disk, as illustrated in Figure 1. A low-density cavity forms due to binary torques, creating a gap between the inner edge of the circumbinary disk and the outer edges of the mini-disks (e.g., P. Artymowicz & S. H. Lubow 1994). Mass accretion proceeds through the circumbinary disk, along two accretion streams, and onto the two mini-disks (e.g., A. I. MacFadyen & M. Milosavljević 2008; B. D. Farris et al. 2014, 2015; C.-S. Yan et al. 2014; D. J. D'Orazio et al. 2016; D. J. Muñoz & D. Lai 2016; R. Miranda et al. 2017; Y. Tang et al. 2018; D. J. Muñoz et al. 2019; J. R. Westernacher-Schneider et al. 2022), while mass transfer between the two mini-disks across the Lagrange point is neglected in this work. Our disk model for the binary system follows previous studies (C. Roedig et al. 2014; D. J. D'Orazio & J. Samsing 2018), but we incorporate mass loss from the disk system to investigate its effect on the emergent spectrum.

In the standard thin-disk model (N. I. Shakura & R. A. Sunyaev 1973), the effective temperature at a distance r from a central BH of mass M accreting at a rate $\dot{M}$ is given by the energy balance between viscous heating and radiative cooling:

$$T_{\rm eff} = \left[\frac{3}{8\pi\sigma_{\rm SB}}\frac{GM\dot{M}}{r^3}\left(1-\sqrt{\frac{r_{\rm in}}{r}}\right)\right]^{1/4}, \tag{1}$$

where $\sigma_{\rm SB}$ is the Stefan–Boltzmann constant, and $r_{\rm in}$ is the disk inner edge, and where the last term inside the parentheses arises from the assumed torque-free inner boundary condition. In our model, the turnover wavelength of the V-shaped SED is set by the temperature contrast between the hottest region in the circumbinary disk and the coldest region in the mini-disks (see Figure 1). To quantify this, we introduce a characteristic temperature T_0, defined at $r = a \sim 10^3\,R_{\rm S}(\gg r_{\rm in})$ as[6]

$$T_0 \simeq 6.3\times 10^3\,\dot{m}^{1/4}M_7^{-1/4}\left(\frac{a}{10^3\,R_{\rm S}}\right)^{-3/4}\ {\rm K}, \tag{2}$$

so that the characteristic photon energy falls in the optical bands. Here, a is the binary semimajor axis, $\dot{m}\equiv\dot{M}/\dot{M}_{\rm Edd}$ is the mass-accretion rate normalized by the Eddington value of $\dot{M}_{\rm Edd}\equiv L_{\rm Edd}/\eta_0 c^2$, $\eta_0 = 0.1$ is the radiative efficiency, $M_7\equiv M/(10^7\,M_\odot)$, and $R_{\rm S}$ is the Schwarzschild radius of the BH. The physical quantities related to the BH mass are defined separately for the primary and secondary BH ($M_1\geqslant M_2\equiv qM_1$) as well as the total mass ($M = M_1 + M_2$). Recent hydrodynamical simulations suggest that most binaries coupled to their circumbinary disks develop eccentricities of $e\sim 0.5$ (D. J. D'Orazio & P. C. Duffell 2021; J. Zrake et al. 2021; M. Siwek et al. 2023). Here, we neglect this complication for simplicity, and assume that binaries are born on orbits with $e\lesssim 0.1$. In this case, the above simulations find that the orbits are rapidly circularized, and we adopt $e = 0$ throughout this study.

We note that in the outer regions of the accretion disk, where the photospheric temperature is low ($T_{\rm eff}\ll 5000$ K), $\rm H^-$ opacity dominates in partially ionized layers, and vertical energy transport is driven by convection (C. Hayashi 1961; R. Hoshi 1979; F. Meyer & E. Meyer-Hofmeister 1982). At larger radii, the optical depth eventually drops below unity, and the assumption of a locally blackbody disk spectrum no longer holds. In this study, we do not account for these effects in the outermost layers, but instead focus on modeling the SED in the UV–optical bands, which can be directly compared to observations.

This temperature T_0 corresponds to the photon energy at the turnover point of the V-shaped SEDs, giving a characteristic turnover wavelength:

$$\lambda_{\rm t} = \frac{hc}{3kT_0} = 0.76\,\dot{m}^{-1/4}M_7^{1/4}\left(\frac{a}{10^3\,R_{\rm S}}\right)^{3/4}\ \mu{\rm m}. \tag{3}$$

The numerical factor of 3 in the denominator depends on the width of the gap created by the binary. We adopt this factor of 3 in our analytical estimate of $\lambda_{\rm t}$, while the full SEDs shown in the figures are obtained by numerically calculating the disk spectrum. Following C. Roedig et al. (2014), we set the inner edge of the circumbinary disk at $r_{\rm in,cbd} = 2a$ and the outer edges of the mini-disks at $r_{\rm out,1} = 0.27q^{-1/3}a$ for the primary and $r_{\rm out,2} = 0.27q^{1/3}a$ for the secondary BH. These truncation radii can be estimated analytically (B. Rudak & B. Paczynski 1981; P. P. Eggleton 1983) and have been verified in many hydrodynamical simulations (e.g., P. Artymowicz & S. H. Lubow 1994; D. J. D'Orazio et al. 2013, 2016; B. D. Farris et al. 2014; S. Mahesh et al. 2024).

For a steady-state accretion disk with a constant mass inflow rate ($\dot{M}\propto r^0$), the effective temperature follows the radial dependence $T_{\rm eff}\propto r^{-3/4}$. This results in a multicolor blackbody spectrum with a spectral slope of $f_\nu\propto\nu^{\alpha_\nu}$, where $\alpha_\nu = 1/3$. This blue spectrum ($\alpha_\nu > 0$) is a well-known prediction of the standard accretion disk model. However, it contradicts the observed spectral index of AGN continua, which is significantly redder, with $\alpha_\nu\simeq -0.44$ (D. E. Vanden Berk et al. 2001). The redder spectral index is attributed to multiple physical effects, including electron scattering being the dominant opacity source over free–free absorption in the inner hot disk, relativistic corrections to both the BH gravitational potential and radiative transfer, and possible dust reddening, all of which collectively modify the spectrum to resemble observed AGN continua (e.g., B. Czerny & M. Elvis 1987; A. Laor & H. Netzer 1989; A. Laor & B. T. Draine 1993).

In this paper, to account for this discrepancy in spectral color, we introduce mass loss from the accretion flow parameterized as $\dot{M}\propto r^p$ ($0\leqslant p < 1$). Under this assumption, the radial dependence of the effective temperature is modified to $T_{\rm eff}\propto r^{-(3-p)/4}$, and the spectral slope becomes $\alpha_\nu = (1–3p)/(3-p)$. For $p\geqslant 1/3$, the spectral index reddens (i.e., $\alpha_\nu\leqslant 0$), bringing it closer to observed AGN continuum spectra (D. E. Vanden Berk et al. 2001). To include this effect, we model the accretion rate as

$$\dot{M}(r) = \dot{M}_0\cdot\max\left[1, \left(\frac{r}{r_{\rm c}}\right)^p\right], \tag{4}$$

where $\dot{M}_0$ is the mass-accretion rate at the innermost disk radius and $\dot{m}_0 = \dot{M}_0/\dot{M}_{\rm Edd}$. We set the transition radius inside which outflows cease to $r_{\rm c} = 10\,R_{\rm S}$. This choice is somewhat arbitrary, but numerical simulations for BH accretion generally find $r_{\rm c}/R_{\rm S}$ to be on the order of $\mathcal{O}(10)$ (e.g., M. A. Abramowicz et al. 2002; F. Yuan & R. Narayan 2014). Using this prescription in Equation (5), the turnover wavelength for $p = 0.5$ is

$$\lambda_{\rm t} = 0.43\,\dot{m}_0^{-1/4}M_7^{1/4}\left(\frac{a}{10^3\,R_{\rm S}}\right)^{5/8}\ \mu{\rm m}, \tag{5}$$

which is close to the Balmer limit wavelength. In Figure 2, we show the relationship between the turnover wavelength of the V-shaped LRD spectrum and the BH mass, assuming $\dot{m}_0 = 1$ and $p = 0.5$. The red shaded region and thick curves indicate the binary separations corresponding to $\lambda_{\rm t}$ = 3000–5000 Å (D. J. Setton et al. 2025a).

The presence of dense ($n\gtrsim 10^8\ {\rm cm}^{-3}$) and moderately fast ($v_{\rm out}\sim 100\ {\rm km\ s}^{-1}$) outflows in LRDs has been inferred from spectral analyses of absorption features superimposed on broad Balmer emission lines (K. Inayoshi & R. Maiolino 2025; V. Rusakov et al. 2026). The high density is required to populate atomic hydrogen in the $n = 2$ state via collisional excitation within the outflow, while the outflow velocity is

---

[6] C. Roedig et al. (2014) measure T_0 at $a = 100\,R_{\rm S}$, but their definition of $R_{\rm S}$ should be half of the Schwarzschild radius.

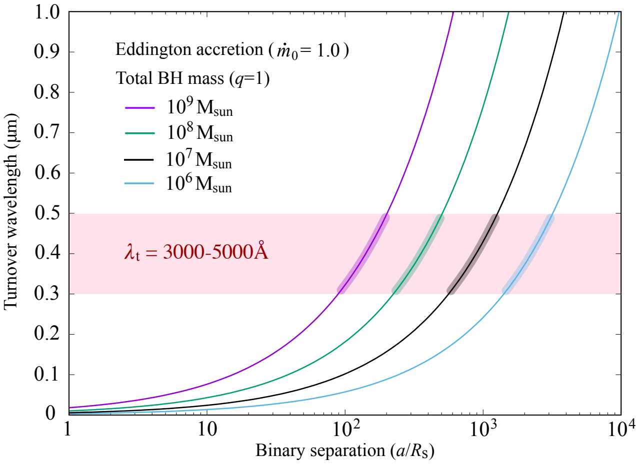

Figure 2. Turnover wavelength ($\lambda_{\rm t}$) characterizing the V-shaped LRD spectrum for each model. The red shaded region and thick curves indicate to the binary separations corresponding to $\lambda_{\rm t} = 3000$–5000 Å.

measured from P Cygni absorption/emission profiles in the observed spectra. The inferred outflow rate is substantially super-Eddington, consistent with numerical predictions for outflows launched from super-Eddington accreting BHs (e.g., H. Hu et al. 2022). Moreover, the weakness of X-ray emission in most LRDs (e.g., H. B. Akins et al. 2025; R. Maiolino et al. 2025) and the double-sided exponential profiles of Balmer emission lines (V. Rusakov et al. 2026) suggest that the central AGNs powering LRDs are deeply embedded within high-column-density media, consistent with super-Eddington inflow/outflow systems (e.g., P. Madau & F. Haardt 2024; A. de Graaff et al. 2025; K. Inayoshi et al. 2025; R. P. Naidu et al. 2025).

The mass-accretion rate through the circumbinary disk is divided into two mini-disks (e.g., D. Lai & D. J. Muñoz 2023). The ratio of the mass-accretion rates generally depends on the mass ratio; namely, $\dot{M}_i = f_i(q)\dot{M}(r)$ for $i = 1,\ 2$ with $f_1 + f_2 = 1$. Numerical simulations show a tendency for the secondary BH, which orbits at a larger distance from the center of mass, to accrete more ($f_1 < f_2$). In this work, we adopt q-dependent ratios, given by

$$f_1 = \frac{1}{2} - \frac{4}{9}(1 - q), \tag{6}$$

and $f_2 = 1 - f_1$ (D. J. Muñoz et al. 2020; D. Lai & D. J. Muñoz 2023). This formula reproduces numerical simulation results for $0.1 \lesssim q \leqslant 1$, and is broadly consistent with other studies (e.g., B. D. Farris et al. 2014; P. C. Duffell et al. 2020; M. Siwek et al. 2023). Using the prescription given in Equation (6) for unequal-mass binaries with $q \simeq 0.1$, the primary BH accretes at $\simeq$10% of the total feeding rate, corresponding to an Eddington ratio of $\dot{M}_1/\dot{M}_{\rm Edd,1} = 0.11\,\dot{m}_0$. We note that the assumption of an optically thick disk is valid only for $\dot{m}_0 \gtrsim 0.1$, above which the accretion flow remains in the standard thin-disk regime (N. I. Shakura & R. A. Sunyaev 1973). Below this threshold, the flow is expected to transition to an optically thin, advection-dominated accretion flow (e.g., F. Yuan & R. Narayan 2014). In this sub-Eddington regime, the big blue bump seen in AGN UV/optical spectra disappears (L. C. Ho 1999), and the accretion energy is instead released as X-ray and radio emission (L. C. Ho 2002, 2008), which are not observed in LRDs (e.g., R. Maiolino et al. 2025). This suggests that LRDs cannot be associated with binaries with very unequal ($q \ll 0.1$) masses; however, such binaries are expected to be a small minority produced in galaxy mergers (e.g., L. Z. Kelley et al. 2017).

For mass accretion near or moderately exceeding the Eddington limit ($\dot{m}_0 \gtrsim 1$), the temperature structure of the mini-disks is characterized by a geometrically thick, slim-disk model. Within the photon-trapping radius, defined as $r_{\rm tr}/R_{{\rm S},i} \lesssim \dot{M}_i(r_{\rm tr})/\dot{M}_{{\rm Edd},i}$, the heat generated by viscosity is advected inward with dense inflows rather than being transported by radiative diffusion (M. A. Abramowicz et al. 1988; S. Kato et al. 2008). The radial profile of the disk surface temperature is given by K.-y. Watarai (2006) as

$$T_{\rm eff} = 7.91 \times 10^6 f^{1/8} M_{i,7}^{-1/4}\mathcal{F}(r,\,\dot{m}_i)\left(\frac{r}{R_{{\rm S},i}}\right)^{-1/2}\ {\rm K}, \tag{7}$$

where f is the ratio of the advection cooling rate to the viscous heating rate[7], and the function $\mathcal{F}$ characterizes the disk inner boundary as $\mathcal{F}(r,\,\dot{m}_i) = [1 - \sqrt{r_{\rm in}/r}\,]^{1/4}$ for $\dot{m}_i < 4$, and $\mathcal{F}(r,\,\dot{m}_i) = 1$ for $\dot{m}_i \geqslant 4$. The radius of the disk inner edge ($r_{\rm in}$) is set to the innermost stable circular orbit (ISCO) radius for a nonspinning BH ($r_{\rm in} = 3\,R_{{\rm S},i}$) for $\dot{m}_i \leqslant 1$, and for $1 < \dot{m}_i < 4$ is calculated with a linear interpolation in the plane of $\log \dot{m}_i - \log r_{\rm in}$ between the ISCO radius and $1.1\,R_{{\rm S},i}$. We note that the surface temperature profile reproduces the conventional form of $T_{\rm eff} \propto r^{-(3-p)/4}$ for the sub-Eddington regime (see Equation (1)).

Figure 3 illustrates the surface temperature profiles around a binary BH with a total mass of $M = 10^7\,M_\odot$, mass ratio $q = 0.1$, orbital separation $a = 300\,R_{\rm S}$, and mass-loss parameter $p = 0.5$, for three components: the primary mini-disk (purple), secondary mini-disk (green), and circumbinary disk (cyan). Each disk component is shown for different mass-accretion rates of $\dot{m}_0 = 1$ (solid), 3 (dashed), and 10 (dotted). The slim-disk model is also applied to the circumbinary disk; however, the temperature structure is well described by the thin-disk model as its inner edge is located outside the photon-trapping radius. The secondary mini-disk and the inner region of the primary mini-disk follow $T_{\rm eff} \propto r^{-1/2}$, where advection cooling dominates radiative cooling.

3. Results

3.1. Parameter Dependence

Figure 4 presents the spectra of a binary BH system with $M = 10^7\,M_\odot$, $q = 0.1$, $\dot{m}_0 = 1.0$, and $p = 0.5$. In the left panel, we show the case for a binary separation of $a = 10^3\,R_{\rm S}$. The attenuation-free SED is decomposed into contributions from the primary mini-disk (purple), secondary mini-disk (green), and circumbinary disk (cyan).

The total SED (black dashed) is dominated by the primary mini-disk in the UV regime and the circumbinary disk in the optical regime, with a turnover wavelength of $\lambda_{\rm t} \simeq 0.4\,\mu$m, consistent with both observations and the analytical estimate in Equation (5). At this binary separation, the optical continuum arises from the Wien tail at the inner edge of the circumbinary disk, while the UV continuum follows the Rayleigh–Jeans tail from the outer edge of the primary mini-disk. Although the

---

[7] The fitting form of the ratio is given by K. Watarai (2006) as $f = 0.5(X^2 + 2 - X\sqrt{X^2 + 2}\,)$, where $X = 0.281r/(\dot{m}R_{\rm S})$.

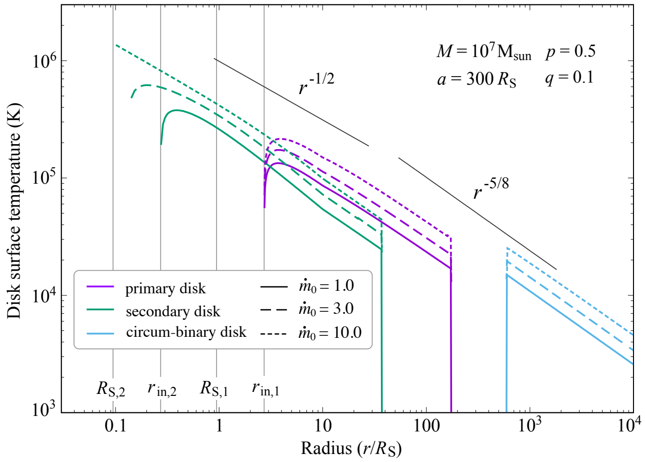

Figure 3. Radial profiles of the surface temperature of accretion disks around a binary BH with a total mass of $M = 10^7\,M_\odot$, mass ratio $q = 0.1$, and orbital separation $a = 300\,R_S$, for three components: the primary mini-disk (purple), secondary mini-disk (green), and circumbinary disk (cyan). Each component is shown for different mass-accretion rates of $\dot{m}_0 = 1$ (solid), 3 (dashed), and 10 (dotted). For the mini-disks, the horizontal axis denotes the radial distance from each BH, normalized by the Schwarzschild radius of the total BH mass. For $1 \leqslant \dot{m}_0 \leqslant 10$, the temperature profiles of both the circumbinary disk and the primary mini-disk follow $T_{\rm eff} \propto r^{-5/8}$, consistent with a thin-disk model including mass loss characterized by $p = 0.5$. The secondary mini-disk follows $T_{\rm eff} \propto r^{-1/2}$ in the slim-disk regime, where advection cooling dominates radiative cooling. Its inner edge shifts depending on the accretion rate (see text).

secondary mini-disk contributes less to the UV luminosity, its spectrum extends to shorter wavelengths at $\lesssim 0.02\,\mu$m with a bluer slope than the primary disk, due to super-Eddington accretion modeled with a slim disk (see Equation (7)). This model naturally produces a V-shaped SED even in the absence of dust attenuation, host-galaxy stellar light, and scattered AGN light.

The black solid curve shows the SED with modest attenuation ($A_V = 0.3$ mag), which suppresses the UV component. This model yields UV and optical slopes of $\beta_{\rm UV} = -1.2$ and $\beta_{\rm opt} = 0$ (gray lines), consistent with the color selection criteria for LRDs (J. E. Greene et al. 2024; J. Matthee et al. 2024; D. D. Kocevski et al. 2025). A key feature of our model is that only a low level of dust attenuation is needed, in contrast to most previous studies of LRD SEDs, which postulate significant obscuration with $A_V \sim$ 3–4 mag. This weaker attenuation also aligns with the weak NIR fluxes observed in LRDs with JWST/MIRI photometry (e.g., H. B. Akins et al. 2025; D. J. Setton et al. 2025b; B. Wang et al. 2025, 2024), as the reprocessed IR radiation should be weaker if the intrinsic SED is UV-faint and redder in the optical bands. In Section 4.2, we discuss an application of our low-attenuation model to the Sołtan argument.

It is worth noting that this spectral model favors a mass ratio of $q \lesssim 0.1$, where the primary accretion fraction f_1 ranges $\simeq$0.055–0.1 (see Equation (6)). Based on the disk energetics argument in Appendix A, the luminosity density ratio between the UV (from the primary mini-disk) and optical (from the circumbinary disk) bands is evaluated in Equation (A5) as

$$\frac{L_{\nu_{\rm UV}}}{L_{\nu_{\rm opt}}} \sim 0.12 \left(\frac{f_1}{0.1}\right)\left(\frac{\nu_{\rm opt}}{0.1\nu_{\rm UV}}\right)\left(\frac{a}{10^3\,R_S}\right)^{1/2}, \tag{8}$$

where $\nu_{\rm UV}$ and $\nu_{\rm opt}$ are the characteristic photon frequencies in the UV and optical bands, respectively. Under these conditions, the resulting SED matches the LRD color selection criteria even without or with moderate dust reddening (see Figure 4). In contrast, as the mass ratio approaches unity, the luminosity density ratio increases to $\sim\mathcal{O}(1)$, leading to a spectrum dominated by the mini-disk. This case fails to reproduce the characteristic V-shaped SED of LRDs, even when dust reddening is considered.

In the right panel of Figure 4, we show how the SED evolves as the binary separation decreases from $a = 10^4$ to $100\,R_S$ (solid curves). For reference, the dashed curves present the circumbinary disk spectra for the largest and smallest separations. For $a = 10^4\,R_S$, the SED at $\lambda \lesssim 1\,\mu$m is dominated by the primary mini-disk, with a red spectral slope of $\alpha_\nu = -1/5$ ($p = 0.5$). As the binary inspirals, the circumbinary disk heats up, increasing its luminosity and shifting the peak flux density to shorter wavelengths. By the time the binary reaches $a = 100\,R_S$, the circumbinary disk fully dominates the SED, and the characteristic V-shaped SED fades, leaving only a red continuum. This spectral evolution in the emergence of a V-shaped SED is observed for different BH masses, although the binary separation differs (see Figure 2).

However, there is a caveat for interpreting this figure. Once the binary separation shrinks below $a \lesssim 600\,R_S$, the orbital decay begins to accelerate due to energy and angular momentum loss via GW radiation. At later stages, the inner edge of the circumbinary disk can no longer follow the rapidly inspiraling binary and instead approximately stalls at the decoupling radius on a viscous timescale (A. J. Dittmann et al. 2023; L. M. Krauth et al. 2023; D. O'Neill et al. 2025; see more discussion in Section 3.3). Thus, the case labeled $a = 100\,R_S$ should be interpreted as the stage at which the inner edge of the circumbinary disk is located at $r_{\rm in,cbd} = 200\,R_S$, rather than the moment when the binary reaches $a = 100\,R_S$.

Numerical simulations have shown that binary BH systems can produce SEDs with a characteristic dip at the wavelength where the spectra of the hot mini-disks intersect with that of the cooler circumbinary disk (e.g., C. Roedig et al. 2014; B. D. Farris et al. 2015; Y. Tang et al. 2018). In these simulations, the binary separation is typically assumed to be $a \ll 10^3\,R_S$, imprinting its dip feature at high photon energies in the UV to X-ray bands. The spectral turnover energy (or wavelength) is described by Equation (3) in the absence of mass loss ($p = 0$). These studies also demonstrate that shock heating powered by the binary orbital energy can significantly enhance the total luminosity and harden the spectrum, often producing strong UV and X-ray features (see also J. R. Westernacher-Schneider et al. 2022 and L. M. Krauth et al. 2023, as well as an earlier study by G. Lodato et al. 2009 proposing that tidal heating of the cavity wall can produce similar effects). However, such high-energy components are generally absent in the redder SEDs of LRDs (e.g., E. Lambrides et al. 2024). Notably, they are also absent in follow-up X-ray observations of optically identified massive binary candidates with both Chandra (M. L. Saade et al. 2020) and XMM-Newton (M. L. Saade et al. 2024). The hard UV/X-ray features can be suppressed in binaries if mini-disks are weak or absent. Recent work suggests that this is indeed the case when the accretion flow is cold (C. Tiede et al. 2025), offering a possible pathway to reconcile binary BH scenarios with LRD observations. Thus far, such high-energy emission from shock-heated accretion streams and mini-disks remains theoretically uncertain, as it depends sensitively on the detailed

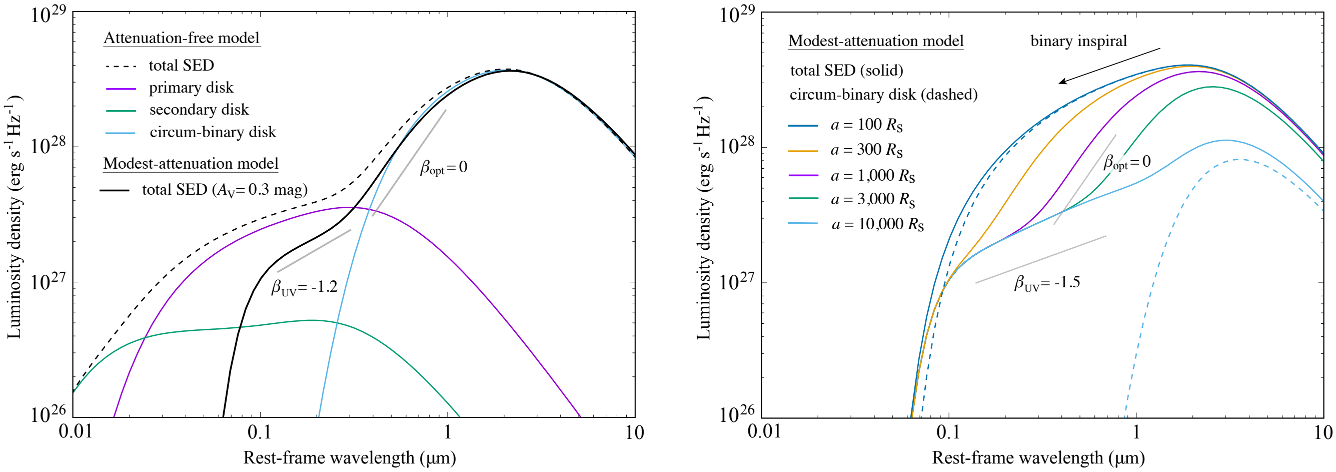

Figure 4. Spectra of a binary BH system with $M = 10^7\,M_\odot$, $q = 0.1$, $\dot{m}_0 = 1.0$, and $p = 0.5$. Left: the case with $a = 10^3\,R_{\rm S}$. The attenuation-free SED is decomposed into contributions from the primary mini-disk (purple), secondary mini-disk (green), circumbinary disk (cyan), and the total system (black dashed). The black solid curve shows the SED with modest attenuation ($A_V = 0.3$ mag), yielding UV and optical slopes of $\beta_{\rm UV} = -1.2$ and $\beta_{\rm opt} = 0$ (gray lines), consistent with the color selection criteria for LRDs. Right: SEDs for various binary separations in the range $a = 10^2$–$10^4\,R_{\rm S}$ (solid curves). For reference, the dashed curves present the circumbinary disk spectra for the smallest and largest separations. As the orbital separation shrinks, the surface temperature of the circumbinary disk increases, shifting the peak wavelength to shorter values.

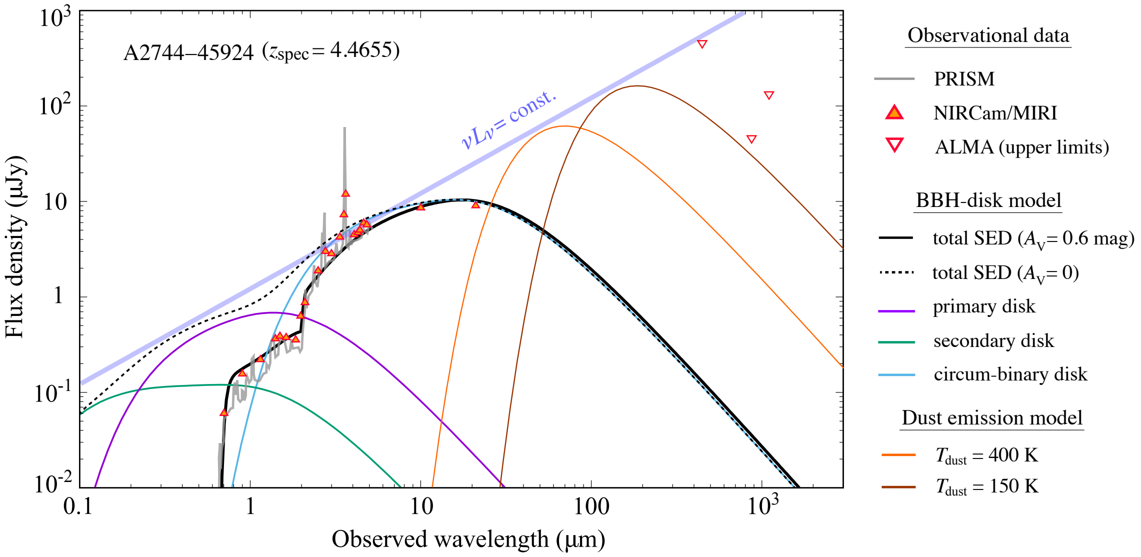

Figure 5. A spectral model for the brightest LRD, A2744-45924, at $z_{\rm spec} = 4.46$, including NIRCam photometry and PRISM data (I. Labbe et al. 2024), as well as MIRI photometry and ALMA flux upper limits (D. J. Setton et al. 2025b). The binary BH-disk SED model assumes parameters $M = 2 \times 10^8\,M_\odot$, $q = 0.1$, $\dot{m}_0 = 3.0$, $p = 0.5$, $a = 300\,R_{\rm S}$, and $A_V = 0.6$ mag, and reproduces the observed SED with only moderate attenuation, as the Wien-tail spectrum of the circumbinary disk is intrinsically red in the rest-frame optical bands. Blackbody spectra with dust temperatures of $T_{\rm dust} = 400$ K (orange) and 150 K (brown) are overlaid, with normalizations chosen to conserve photon energy. Given that the total IR luminosity is limited to $\sim 2 \times 10^{11}\,L_\odot$, the IR spectrum of warm-dust emission is compatible with the MIRI and ALMA observations.

disk thermodynamics and morphology as well as the binary orbital dynamics. Given these uncertainties, we do not explicitly include these components in our model, but instead focus on the more robust emission from the circumbinary disk, which dominates the red optical continua observed in LRD spectra and is less affected by the complex inner-disk physics.

3.2. Case Studies

Figure 5 demonstrates that our binary BH-disk model explains the SED of the brightest LRD (A2744-45924; I. Labbe et al. 2024). A2744-45924 has been confirmed as a broad-line AGN at $z_{\rm spec} = 4.46$ with a Balmer-break feature detected in its PRISM spectrum (J. E. Greene et al. 2024). Follow-up observations have revealed the properties of its emission lines (I. Labbe et al. 2025) and dust emission through MIRI and Atacama Large Millimeter/submillimeter Array (ALMA) observations (D. J. Setton et al. 2025b). Spectral fitting by I. Labbe et al. (2024) indicates strong attenuation ($A_V = 2.4$–3.0 mag), leading to an estimated BH mass of $M_{\rm BH} = 7 \times 10^8\,M_\odot$ via the single-epoch method based on broad Hα emission.

We present a binary BH-disk SED model with parameters $M = 2 \times 10^8\,M_\odot$, $q = 0.1$, $\dot{m}_0 = 3.0$, $p = 0.5$, and $a = 300\,R_{\rm S}$. This model reproduces the observed SED of A2744-45924 with only moderate attenuation ($A_V = 0.6$ mag), as the Wien-tail spectrum of the circumbinary disk is intrinsically red in the rest-frame optical bands. The Balmer-break feature in the model SED is added by using the analytical form based on the

AGN transmitted spectrum with a hydrogen column density of $N_{\rm H} = 10^{23}\,{\rm cm}^{-2}$ (K. Inayoshi & R. Maiolino 2025; see more details in Appendix B). The orbital separation of $a = 300\,R_{\rm S}$ aligns with the values highlighted in Figure 2, ensuring a V-shaped SED with a turnover near the Balmer limit. Although I. Labbe et al. (2024) estimate the BH mass as $M_{\rm BH} = 7 \times 10^8\,M_\odot$ assuming $A_V = 2.4$–3.0, our model suggests a lower total BH mass of $M_{\rm BH} = 2 \times 10^8\,M_\odot$ but with a modest super-Eddington accretion rate of $\dot{m}_0 = 3$. This combination maintains the observed optical luminosity while ensuring that the turnover wavelength $\lambda_{\rm t}$ remains within the LRD selection window. Importantly, the observed flux density is not treated as a free parameter but rather emerges self-consistently from the intrinsic energetics of the accretion disks. We note that these parameters reproducing the observed spectrum of A2744-45924 are not obtained from a fitting procedure. Instead, this work focuses on the model prescription and its physical implications, while the details of a dedicated fitting methodology are left to future work.

Our binary BH-disk model can also explain the SED of another recently reported LRD, MoM-BH*-1 (R. P. Naidu et al. 2025). This object shows the strongest Balmer break among all spectroscopically observed LRDs. This feature cannot be explained by stellar populations alone but likely arises from absorption by dense gas surrounding the nuclear BH (e.g., K. Inayoshi & R. Maiolino 2025; X. Ji et al. 2025). R. P. Naidu et al. (2025) suggest that MoM-BH*-1 represents a super-Eddington accreting BH embedded within an extremely dense, possibly dust-poor gas environment. Such a surrounding medium could resemble a quasi-star (M. C. Begelman et al. 2006, 2008) or hyper-Eddington accretion flows (K. Inayoshi et al. 2016; E. Takeo et al. 2020), characterized by a sufficiently low photospheric temperature of $T_{\rm ph} \sim 5000$–7000 K (C. Hayashi 1961). These interpretations align with our model, in which the inner edge of the circumbinary disk attains a similar surface temperature (see also a BH envelope model proposed in D. Kido et al. 2025).

A key advantage of our binary BH-disk model is that only modest attenuation is required to reproduce the observed SED. This moderate reddening is further supported by the recent discovery of several LRDs showing prominent Balmer breaks (e.g., A. de Graaff et al. 2025; R. P. Naidu et al. 2025; A. J. Taylor et al. 2025b). This, in turn, implies that the intrinsic rest-frame UV emission is not particularly strong, resulting in only moderate NIR flux from reprocessed dust emission. To illustrate this, we overlay blackbody spectra with dust temperatures of $T_{\rm dust} = 400$ K (orange) and 150 K (brown), with normalizations chosen to conserve photon energy. Given that the total IR luminosity is limited to $\sim 2 \times 10^{11}\,L_\odot$, the allowed dust temperature range is $T_{\rm dust} \sim 150$–400 K. In contrast, if the intrinsic UV emission were significantly brighter, the range of dust temperatures required to match MIRI and ALMA constraints would be much narrower. This result is crucial, as a significant fraction of LRDs exhibit faint rest-frame NIR (MIRI bands) and FIR (ALMA bands) fluxes, suggesting the absence of hot, dusty tori in their nuclei and minimal ongoing star formation.

3.3. Evolution of Binary BHs and their SEDs

In our scenario, the binary orbital evolution governs the spectral evolution. Figure 6 summarizes the key timescales and characteristic binary separations for various total BH masses.

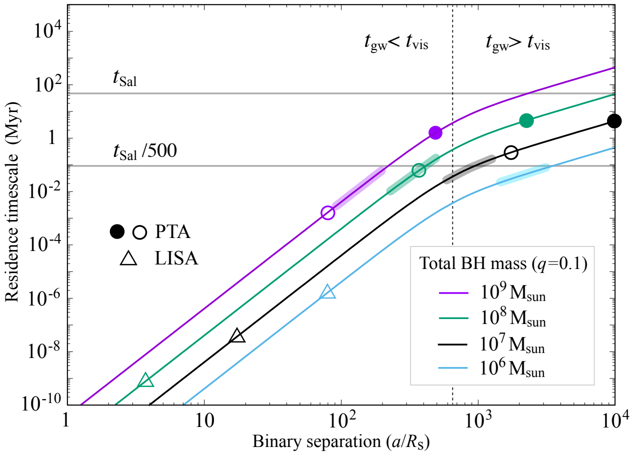

Figure 6. Binary residence time as a function of binary separation for different total BH masses: $M_{\rm BH} = 10^6\,M_\odot$ (cyan), $10^7\,M_\odot$ (black), $10^8\,M_\odot$ (green), and $10^9\,M_\odot$ (purple). Equal-mass ratio BHs accreting at the Eddington rate for the total mass are assumed. For each curve, the filled circle, open circle, and triangle mark the epochs when the GW frequency reaches $f_{\rm gw} = 2$ nHz, 32 nHz ($=1\,{\rm yr}^{-1}$), and 0.032 mHz, corresponding to the frequency ranges probed by pulsar timing array (PTA) experiments and LISA. The vertical line indicates the transition where binary orbital decay becomes dominated by GW emission rather than interactions with the gaseous disk. The thick curves present the binary separations where $\lambda_{\rm t} = 3000$–5000 Å.

At wider separations, the binary orbital evolution is primarily governed by interactions with the surrounding gas disk. If the secondary BH opens a gap in the disk, its evolution proceeds via type II migration on a viscous timescale (e.g., D. N. C. Lin & J. Papaloizou 1979, 1986; P. J. Armitage & P. Natarajan 2002):

$$t_{\rm vis} = \frac{1}{\alpha\Omega}\left(\frac{a}{H}\right)^2 \simeq 0.14\ {\rm Myr}\ \alpha_{0.01}^{-1} M_7 \left(\frac{a}{10^3\,R_{\rm S}}\right)^{3/2}, \tag{9}$$

where we assume a geometrically thin disk with a scale-height of $H/a = 0.01$ and a α-viscous parameter of $\alpha = 0.01$, consistent with magneto-hydrodynamic simulations (e.g., S. A. Balbus & J. F. Hawley 1998; J. M. Stone & J. E. Pringle 2001; X.-N. Bai 2011). Z. Haiman et al. (2009) provide a more detailed analytical treatment of the disk structures and orbital decay within AGN, but our simple approach with a constant H/a ratio captures the overall trend.

As the binary separation shrinks, GW emission takes over driving the orbital decay through its orbital energy and angular momentum loss on a timescale:

$$t_{\rm gw} \simeq 0.14\ {\rm Myr}\ q_s^{-1} M_7 \left(\frac{a}{10^3\,R_{\rm S}}\right)^4 \tag{10}$$

(e.g., P. C. Peters & J. Mathews 1963), where $q_s \equiv 4q/(1+q)^2$ is the symmetric mass ratio. Figure 6 presents the residence timescale defined as $t_{\rm res}^{-1} \equiv t_{\rm vis}^{-1} + t_{\rm gw}^{-1}$ (solid curves).

By equating the GW and viscous timescales ($t_{\rm gw} = t_{\rm vis}$), we obtain the critical orbital separation at which GW emission begins to dominate the binary inspiral evolution:

$$a_{\rm gw}^{\rm vis} \simeq 6.5 \times 10^2\, q_{s0}^{2/5} \alpha_{0.01}^{-2/5}\, R_{\rm S}, \tag{11}$$

where $q_{s0} = q_s/0.33$ is the symmetric mass ratio normalized by the value for $q = 0.1$. The corresponding GW frequency (i.e., twice the orbital frequency) in the source frame is calculated by

$$f_{\rm gw} \simeq 71.8\,{\rm nHz}\,M_7^{-1}\left(\frac{a}{10^3\,R_{\rm S}}\right)^{-3/2}. \quad (12)$$

For lower-mass BHs ($M_{\rm BH} \lesssim 10^7\,M_\odot$), the binary enters the frequency range detectable by the PTA experiments (filled and open circles in Figure 6), while its orbital evolution is still driven by disk viscosity. As the binary inspirals further and exits the PTA band, the characteristic V-shaped SED feature emerges (the shaded region on each curve in Figure 6). In contrast, for more massive BHs ($M_{\rm BH} \gtrsim 5 \times 10^7\,M_\odot$), the binary remains within the PTA-detectable GW frequency range even when the LRD signature becomes observable. We note that the separation range where the GW and LRD signatures coexist extends further for high-redshift sources, as the circle symbols shift by a factor of $\sim 3\,[(1+z)/6]^{-2/3}$. Eventually, these inspiraling binaries enter the frequency band at $f_{\rm gw} \simeq 0.032$ mHz (triangle symbols), corresponding to the ranges probed by the Laser Interferometer Space Antenna (LISA).

The duration of the LRD phase, when the spectral properties match the color selection criteria, corresponds to only ∼0.2% of the Eddington-limited accretion e-folding timescale (i.e., the Salpeter timescale, $t_{\rm Sal}$). Taking the Salpeter timescale as a reference for the AGN lifetime, the duty cycle of LRD spectral features increases when the viscous timescale is longer. This can occur due to inefficient turbulent viscosity ($\alpha < 0.01$) and/or even thinner disk configurations ($H/a < 0.01$). This suggests that the majority of accretion activity for these BHs occurs during normal AGN phases, when the binary separation is larger and the residence time is longer. As shown in Figure 4, the SED shape at separations of $a \sim 10^4\,R_{\rm S}$ resembles that of the typical unobscured AGNs. A more quantitative discussion of the abundance of this "proto-LRD" population is presented in Section 4.1.

It is worth noting that the dynamics of the circumbinary disk decouples from the binary evolution when $a \ll a_{\rm gw}^{\rm vis}$. At this stage, GW radiation rapidly drives the binary inspiral, while the inner edge of the circumbinary disk remains nearly stationary, unable to adjust on such a short timescale. As a result, the characteristic red optical spectrum originating from the circumbinary disk persists for a duration of $t_{\rm vis} \simeq 74\,M_7$ kyr. Meanwhile, the spectra of the two mini-disks evolve much faster on the GW-driven inspiral timescale. For instance, at $a \lesssim 0.4\,a_{\rm gw}^{\rm vis} \sim 260\,R_{\rm S}$, the GW timescale is an order of magnitude shorter than the viscous timescale.

In this decoupling regime, strong binary torques have been proposed to compress the disk inside the secondary orbit (P. J. Armitage & P. Natarajan 2002). This GW-driven disk squeezing triggers rapid accretion onto the primary BH and potentially produces a luminous precursor event (e.g., P. Chang et al. 2010; A. Cerioli et al. 2016; C. Fontecilla et al. 2017)—days to hours before the BH merger in the source frame. If the squeezing process continues until the binary reaches $a \simeq 20\,R_{\rm S,1}$, the inner mini-disk becomes geometrically thick ($H/a \sim 1$) and envelops the compact binary system within a nearly spherical structure (C. Fontecilla et al. 2017). By this stage, the accretion rate onto the primary BH increases significantly, scaling as $t_{\rm vis}/t_{\rm gw} \sim \mathcal{O}(100)$. However, due to efficient photon trapping, the increase in radiative luminosity is limited to a factor of a few (e.g., M. A. Abramowicz et al. 1988; K. Ohsuga et al. 2005; Y.-F. Jiang et al. 2014; A. Sądowski et al. 2015). On the other hand, recent high-resolution simulations suggest an alternative picture in which the mini-disks are tidally disrupted and depleted prior to merger, rather than squeezed (L. M. Krauth et al. 2023). In this scenario, the UV/X-ray emission drops by four orders of magnitude as the binary evolves.[8] These contrasting outcomes highlight the theoretical uncertainty regarding the final stages of binary disk interaction.

Finally, following the merger, the remnant BH receives a recoil kick opposite to the direction of GW emission. This motion induces prompt shocks between the disk material bound to the recoiling remnant and the outer disk, potentially generating an observable electromagnetic counterpart (Z. Lippai et al. 2008; J. D. Schnittman & J. H. Krolik 2008; M. Megevand et al. 2009; M. Anderson et al. 2010; L. R. Corrales et al. 2010; E. M. Rossi et al. 2010).

4. Discussion

4.1. Abundance

The high abundance of LRDs in a given cosmic volume is an intriguing aspect of this population, with a comoving number density of $\phi \simeq 10^{-5}$–$10^{-4}\,{\rm Mpc}^{-3}$. This is approximately ∼1–2 orders of magnitude higher than that of UV-bright quasars, but occupies $\lesssim 10\%$ of unobscured broad-line AGNs (Y. Harikane et al. 2023; R. Maiolino et al. 2024; A. J. Taylor et al. 2025a) and possibly ∼1% of obscured Type 2 AGNs (which lack broad emission lines, and are selected based on narrow line emission diagnostics; J. Scholtz et al. 2025) in the same redshift range.

In our scenario, the spectral features of LRDs originate from binary BHs at orbital separations of $a \simeq 10^3\,R_{\rm S}$. However, the majority of accretion activity for these BHs occurs in normal AGN phases, when the binary separation is wider and thus the residence time is longer. At separations of $10^3 \lesssim a/R_{\rm S} \lesssim 10^4$, the SED[9] resembles that of typical AGNs and does not show the distinctive V shape seen in LRDs, while retaining a similar UV magnitude (see the right panel of Figure 4). In this regime, binaries are coupled well to the circumbinary disk, and thus their residence time is expected to be governed roughly by the viscous time $t_{\rm vis}(\propto a^{3/2})$. Given the observed abundance ratio between LRDs and unobscured AGNs with comparable UV magnitudes, a factor of ∼30 difference in number density (e.g., V. Kokorev et al. 2024a; D. D. Kocevski et al. 2025), the abundance of normal AGNs can be explained by a population of binary BHs at separations of $a \simeq 10^4\,R_{\rm S}$ in our scenario.

Observationally, LRDs peak in abundance at $z \sim 6$ and decline sharply toward $z \lesssim 4$ (D. D. Kocevski et al. 2025; Y. Ma et al. 2025). This redshift evolution reflects the transient nature of LRDs with a characteristic fading timescale of $t_{\rm LRD} \lesssim 1$ Gyr. K. Inayoshi (2025) proposed that LRD phases correspond to the initial episode of AGN triggering processes and their unique features fade during the subsequent episodes

---

[8] A recent GRMHD simulation (L. Ennoggi et al. 2025) finds a similar destruction of the mini-disks just prior to merger, but does not find a drop in the total bolometric luminosity, which is dominated by a large Poynting flux.

[9] The rest-frame UV-to-optical emission is primarily produced by the two mini-disks, as shown in Figure 4. At these large separations, the surface temperature of the circumbinary disk is not determined by radiative cooling but by convective heat transport (R. Hoshi 1979; S. Mineshige & Y. Osaki 1983). As the binary separation increases further, the circumbinary disk becomes optically thin. We do not model this regime in this work.

as the system transitions into a typical AGN phase. In our scenario, the activity of LRDs (more generally, AGNs) is driven by mergers of dark-matter halos and/or galaxies that host massive BHs. Assuming a linear BH-to-halo mass relation, the BH mass ratio required to reproduce LRD spectra ($q \lesssim 0.1$; see Equation (8) and discussion in Section 3.1) is naturally achieved through minor mergers of halos. Such mergers are frequent in cosmological N-body simulations, with merger rates per halo per unit redshift of order unity or higher for $q \lesssim 0.1$ (O. Fakhouri et al. 2010), resulting in the emergence of LRDs in the early universe.

How do LRDs lose their characteristics within this framework? One possible explanation is that their compact morphologies are disrupted by stellar mass build-up during subsequent mergers with normal galaxies. Star formation and stellar mass accumulation driven by these mergers could cause the AGN host to appear more extended. Blending stellar components with the underlying AGN eases their unique LRD features. K. Inayoshi (2025) showed that a merger frequency of $p \gtrsim 0.5$ per halo per redshift interval (corresponding to mergers with $q \lesssim 0.1$) can quantitatively explain the rapid declining trend of the LRD population (see also F. M. Khan et al. 2025).

4.2. Sołtan Argument

This scenario suggests that LRDs are not heavily obscured AGNs, but instead exhibit moderate extinction ($A_V \lesssim 1$ mag). Such weak reddening is further supported by the recent discovery of several LRDs showing a prominent Balmer break (e.g., R. P. Naidu et al. 2025; A. de Graaff et al. 2025; A. J. Taylor et al. 2025b). As a result, the intrinsic luminosity estimates for the entire LRD population are revised from $A_V \simeq 3$–4 to $A_V \lesssim 1$ mag. This modification decreases the inferred intrinsic luminosity by a factor of ~ 10 ($\equiv 10^{\Delta A_V/2.5}$), where ΔA_V represents the difference in attenuation between our model and those adopted in previous studies that assume heavy dust reddening (e.g., Y. Harikane et al. 2023; D. D. Kocevski et al. 2023; J. E. Greene et al. 2024; J. Matthee et al. 2024; V. Kokorev et al. 2024b; B. Wang et al. 2024; H. B. Akins et al. 2025). If this is the case, the luminosity density of LRDs is reduced by the same factor of 10, and the corresponding BH mass density decreases by a factor of ~ 3, given that single-epoch virial mass estimates follow $M_{\rm BH} \propto L^{1/2}$, assuming the broad-line region luminosity–size empirical relation calibrated via reverberation mapping for nearby AGNs. Consequently, the radiative efficiency required to reconcile the BHAD with the BH mass density for LRDs is reduced by a factor of ~ 3 ($= 10^{\Delta A_V/5.0}$), making it consistent with the canonical 10% radiative efficiency (Q. Yu & S. Tremaine 2002; I. Delvecchio et al. 2014; Y. Ueda et al. 2014) and thereby resolving the apparent tension with the classical Sołtan argument (K. Inayoshi & K. Ichikawa 2024).

4.3. Variability

Flux variability is a key observational feature supporting the AGN origin of LRDs. Based on limited multiepoch observations (typically two or three visits per source), to date UV and optical data have revealed little or no significant variability among JWST-identified AGNs, including LRDs (M. Kokubo & Y. Harikane 2025). An extended variability analysis using a larger sample of ~ 300 LRDs from publicly available photometric data also finds that most LRDs show no detectable variability on observational timescales, although eight sources are identified as variable LRD candidates with significant flux changes (Z. Zhang et al. 2025). Furthermore, some LRDs with spectroscopically confirmed broad Balmer emission lines exhibit variability on year-long timescales (L. J. Furtak et al. 2025; X. Ji et al. 2025).

In our model, flux variability arises from several components of the binary disk system. These include the orbital motion of the mini-disks and the interaction between shock-heated gas streams and both the outer edges of the mini-disks and the inner edge of the circumbinary disk (e.g., B. D. Farris et al. 2015; D. J. Muñoz & D. Lai 2016; R. Miranda et al. 2017; Y. Tang et al. 2018). Such interactions naturally produce multiwavelength flux variations with strong periodicity, particularly at twice the binary orbital frequency, with significant and distinctive chromaticity (J. R. Westernacher-Schneider et al. 2022). As a result, periodic variability on the timescale of $\sim 2[(1+z)/5]M_7$ yr in the observer frame emerges naturally when the binary separation is $a \sim 10^3\,R_{\rm S}$ (see Equation (12)), the regime in which the characteristic LRD spectral features become prominent and persist over timescales of ~ 0.1–1 Myr (see Figure 6). Confirming such periodicity will require multiyear baselines. However, Doppler modulation would produce periodic variability in phase with any possible periodic redshift/blueshift of emission lines arising from the mini-disks (e.g., Fe Kα lines; B. McKernan et al. 2013). Spectroscopic time-domain observations could confirm these correlated continuum and line-shift modulations, even with a baseline shorter than a full period.

For simplicity, as mentioned above, we assume that the binary orbit remains circular throughout the evolution from the early binary–disk coupling phase to the final merger. This assumption is justified because GW emission efficiently damps eccentricity during the late inspiral phase (P. C. Peters & J. Mathews 1963). However, hydrodynamic simulations suggest that gas-driven interactions can excite and maintain orbital eccentricity (J. Zrake et al. 2021; M. Siwek et al. 2023), which potentially remain at moderate values of $e \sim \mathcal{O}(0.1)$ at the separations of $a \sim 10^3\,R_{\rm S}$ relevant to LRD formation. Nonzero eccentricity can further modulate the light curves, introducing bursty signatures associated with accretion spikes near periapse (J. R. Westernacher-Schneider et al. 2022). Future investigation is needed to examine the detailed connection between binary motion and the variability feature of LRDs within this framework.

4.4. Multimessenger Observations for LRDs: Implications to Cosmology

An intriguing question is whether binary BHs in the LRD phases can eventually be detected as GW sources. Figure 7 presents the GW spectra for nonspinning BH mergers with a mass ratio of $q = 0.1$, assuming two representative chirp masses of $\mathcal{M} = 10^6$ and $10^7\,M_\odot$, located at redshifts $z = 4$ and 5, respectively. Each spectrum starts 1 yr before merger, and is shown alongside the sensitivity curves of space-based GW detectors, LISA (black), and TianQin (gray; P. Amaro-Seoane et al. 2023; E.-K. Li et al. 2025a).

Binary BHs capable of producing LRD-like SEDs are expected to emit GW signals detectable by both LISA and TianQin during their final inspiral phases. The higher-mass case ($\mathcal{M} = 10^7\,M_\odot$) generates a GW signal that enters the detector frequency bands near the merger and ringdown phases, while the lower-mass system ($\mathcal{M} = 10^6\,M_\odot$) may be observable over a longer duration from early inspiral to final

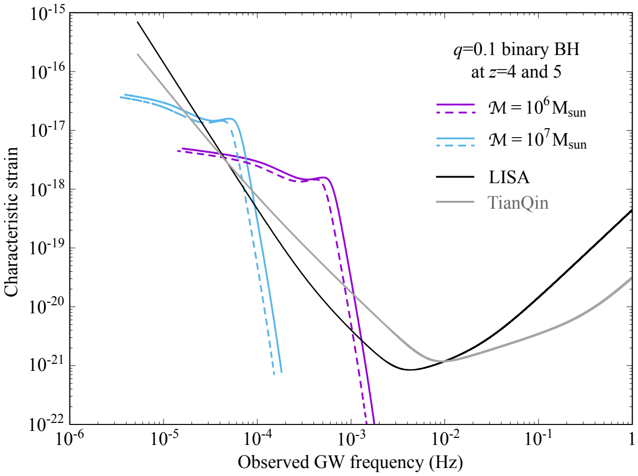

Figure 7. GW spectra for nonspinning BH mergers with a mass ratio of $q = 0.1$, assuming two representative chirp masses of $\mathcal{M} = 10^6$ (purple) and $10^7\,M_\odot$ (cyan), located at redshifts $z = 4$ (solid) and $z = 5$ (dashed), respectively. The sensitivity curves of LISA (black) and TianQin (gray) are overlaid.

coalescence. The GW detectability improves with increasing mass ratio toward unity, as the signal shifts to higher frequencies. However, such nearly equal-mass binaries are unlikely to reproduce the distinct LRD SED, which appears to favor $q \sim 0.1$. In contrast, systems with significantly smaller mass ratios ($q \ll 0.1$) may still preserve the LRD-like SED, depending on the partition of the accretion rate between the two BHs (i.e., f_1 and f_2) for $M \simeq 10^{6-8}\,M_\odot$, but their GW signals shift below the low-frequency sensitivity limits of both detectors, making detection challenging.

As the binary orbit decays, the system eventually loses its distinct LRD features and enters a regime in which it emits GWs detectable by LISA or TianQin. However, this GW-emitting phase lasts much shorter than the LRD phase. For our fiducial case of binary BHs with $M = 10^7\,M_\odot$ and $q = 0.1$ at $z \simeq 4$–5, corresponding to a redshifted chirp mass of $\mathcal{M}_z = 2 \times 10^6(1 + z)\,M_\odot$, only a small fraction, $\mathscr{F} \sim 10^{-6}(1 + z)^{-8/3}$, of such binaries are expected to enter the LISA-detectable frequency band at $f_{\rm gw,min} \gtrsim 0.03$ mHz (see Figures 6 and 7). The binary coalescence time in the observer frame at this frequency is

$$\tau_{\rm gw} \simeq 0.04~{\rm yr}\left(\frac{\mathcal{M}_z}{1.2 \times 10^7\,M_\odot}\right)^{-5/3}\left(\frac{f_{\rm gw,min}}{0.03~{\rm mHz}}\right)^{-8/3}. \quad (13)$$

Given the observed sky surface density of LRDs, $\Sigma_{\rm LRD} \sim 2400~{\rm deg}^{-2}$ (D. D. Kocevski et al. 2025), the expected event rate of high-z GW-detectable binaries originating from LRDs over the full sky ($\mathcal{A} \simeq 40,000~{\rm deg}^2$) is estimated as $\mathscr{R} \simeq f_{\rm bin}\Sigma_{\rm LRD}\mathcal{A}\mathscr{F}/\tau_{\rm gw}$, or

$$\mathscr{R} \simeq 19 f_{\rm bin}~{\rm yr}^{-1}\left(\frac{\mathcal{M}}{2 \times 10^6\,M_\odot}\right)^{5/3}\left(\frac{1 + z}{6}\right)^{-1} \times\left(\frac{f_{\rm gw,min}}{0.03~{\rm mHz}}\right)^{8/3}\left(\frac{\Sigma_{\rm LRD}}{2,400~{\rm deg}^{-2}}\right)\left(\frac{\mathcal{A}}{40,000~{\rm deg}^2}\right), \quad (14)$$

assuming that all LRDs arise from binary BHs (i.e., $f_{\rm bin} = 1$). For a lower total BH mass of $M = 10^6\,M_\odot$, the fraction of $\mathscr{F}$ increases by a factor of $\sim$50, compensating for the $\mathcal{M}^{5/3}$ dependence of the coalescence time. As a result, the expected event rate remains comparable to $\sim 10 f_{\rm bin}~{\rm yr}^{-1}$. This rate is broadly consistent with theoretical predictions from previous studies in the literature based on cosmological galaxy simulations (L. Z. Kelley et al. 2019; M. Volonteri et al. 2020; C. A. Dong-Páez et al. 2023), merger-tree-based semi-analytical models (A. Ricarte & P. Natarajan 2018; E. Barausse et al. 2020; H. Liu & K. Inayoshi 2025), and estimates calibrated by the abundance of low-redshift quasars (C. Xin & Z. Haiman 2021).

The Legacy Survey of Space and Time (LSST) at the Vera C. Rubin Observatory offers an ideal platform for identifying electromagnetic counterparts to GW sources originating from former LRD systems. With more than five million exposures, LSST is collecting time-domain data across a deep, panoramic view of $\sim$18,000 deg^2 of the sky (Ž. Ivezić et al. 2019),[10] yielding an expected detection rate for such rare events of $\mathscr{R} \sim 9 f_{\rm bin}~{\rm yr}^{-1}$, depending on the binary fraction. This estimate represents an upper limit, as the actual detection number is likely lower due to LSST's single-visit detection limit of $\sim$25 mag in the g and r bands. Reaching the brightness of typical faint AGNs identified by JWST (e.g., CEERS 2782 at $z_{\rm spec} = 5.242$ with $\sim$26 mag; D. D. Kocevski et al. 2023) therefore requires $\gtrsim$10 visits. Consequently, the realistic detection rate of such binaries in joint observational programs is expected to be as low as $\sim\mathcal{O}(1)~{\rm yr}^{-1}$, broadly consistent with the predicted number of ultracompact (orbital periods $\lesssim$1 day) binary quasars computed from the luminosity function of low-redshift quasar populations (C. Xin & Z. Haiman 2021, 2024). A synergistic joint observation campaign with the Roman Space Telescope (D. Spergel et al. 2015),[11] utilizing deeper multiband photometric follow-up of LSST-identified candidates, is expected to improve detectability.

4.5. Stochastic GW Background

Another prediction of this scenario is the production of a stochastic gravitational wave background (GWB) from the entire AGN population. The characteristic GWB strain can be calculated as

$$h_{\rm c}^2 = \frac{4}{3\pi^{1/3}}\frac{(G\mathcal{M})^{5/3}}{c^2 f_0^{4/3}}N_0\langle(1 + z)^{-1/3}\rangle \quad (15)$$

(E. S. Phinney 2001), where f_0 is the GW frequency in the observed frame, $N_0 = \int_0^\infty N(z)dz$ is the present-day comoving number density of merged remnants, and $N(z)$ is the event rate density per redshift bin between $z_{\rm min}$ and $z_{\rm max}$. The averaged redshift factor is defined as

$$\langle(1 + z)^{-1/3}\rangle = \frac{1}{N_0}\int_{z_{\rm min}}^{z_{\rm max}}\frac{N(z)}{(1 + z)^{1/3}}dz. \quad (16)$$

We note that the formula in Equation (15) is valid under the assumption that the orbital evolution of the binary is dominated by GW emission rather than viscous torques. This condition is typically satisfied for more massive binary BHs with tighter separations (see the binary–disk decoupling conditions in Figure 6). Furthermore, if the binary orbit is eccentric, GW energy is emitted more efficiently at higher frequencies (e.g.,

---

[10] https://www.lsst.org/scientists/survey-design

[11] https://science.nasa.gov/mission/roman-space-telescope/

M. Enoki & M. Nagashima 2007; A. Sesana 2013; D. J. D'Orazio et al. 2015), though our analysis treats only circular orbits (see also discussion in Section 4.3). The integration range is chosen to include the range $z_{\rm LRD} \simeq 4$–8, where the LRD occurrence rate peaks, yielding the GWB strength as

$$h_{\rm c} \simeq 5.6 \times 10^{-17}\left(\frac{\mathcal{M}}{10^7\,M_\odot}\right)^{5/6}\left(\frac{f_0}{30\ {\rm nHz}}\right)^{-2/3} \times \left(\frac{N_0}{10^{-3}\ {\rm Mpc}^{-3}}\right)^{1/2}\left(\frac{\langle(1+z)^{-1/3}\rangle}{0.522}\right)^{1/2}. \tag{17}$$

Here, we assume that all LRDs originate from binary BHs, representing a certain fraction of the bulk AGN population, including both unobscured and obscured Type 2 AGNs, with a total comoving number density of $N_0 = 10^{-3}\ {\rm Mpc}^{-3}$.

The predicted GWB contribution from binary BHs powering LRDs accounts for $\sim$2% of the observed strain amplitude $A_{\rm GWB} = 2.4^{+0.7}_{-0.6} \times 10^{-15}$ (median with 90% credible interval) at a reference frequency of $1\ {\rm yr}^{-1}(=32\ {\rm nHz})$, as reported by the NANOGrav 15 yr dataset (G. Agazie et al. 2023a, 2023b). This is consistent with the recent conclusion in Á. Kis-Tóth et al. (2025), who showed that if all AGNs are associated with mergers, the resulting GWB amplitude roughly matches observations, dominated by AGNs with BH masses of $\sim 10\,M_\odot$ at redshifts $z \sim 2$. The relatively low GWB amplitude from LRDs reflects the modest masses of binary BHs; even at the high end, their chirp masses only reach $\mathcal{M} \sim 10^7\,M_\odot$. However, if this BH population undergoes further mass growth and experiences major mergers (e.g., reaching $\mathcal{M} \gtrsim 10^9\,M_\odot$) in later epochs through gas-rich galaxy interactions, observed as (ultra-)luminous IR galaxies (e.g., S. Veilleux et al. 2002; I. Delvecchio et al. 2014), the resulting GWB amplitude could approach the levels detected by PTA experiments. This scenario predicts a GWB characteristic strain at $f_0 = 1\ {\rm yr}^{-1}$ of $h_{\rm c} \simeq (1.24 \pm 0.29) \times 10^{-15}$ (K. Inayoshi et al. 2018), consistent with PTA measurements.

5. Summary

In this paper, we propose a scenario in which the V-shaped SED of LRDs originates from a binary BH system, where each BH is surrounded by a circum-BH mini-disk and embedded within a larger circumbinary disk. In this model, the mini-disks have higher effective temperatures, while the circumbinary disk remains cooler. At a critical binary separation of $a \lesssim 10^3\,R_{\rm S}$, the red optical emission arises from the Wien tail of a $T \simeq 5000$ K blackbody at the inner edge of the circumbinary disk, whereas the UV continuum is powered by the mini-disks. Binary torques carve out a gap between the circumbinary disk and mini-disks, setting the turnover wavelength of the V-shaped SED near the Balmer limit.

This configuration naturally reproduces LRD spectra without requiring strong dust attenuation ($A_V \lesssim 1$ mag). As an example, we apply the SED model to A2744-45924, the brightest known LRD at $z_{\rm spec} = 4.46$, which is well constrained by JWST/NIRCam and MIRI, PRISM spectra, and ALMA upper limits (J. E. Greene et al. 2024; I. Labbe et al. 2025; D. J. Setton et al. 2025b). The model successfully fits its observed SED with only moderate extinction ($A_V = 0.6$ mag), significantly lower than previous estimates requiring $A_V > 2$ mag. While a more extensive application to the full LRD population is left for future work, this paper instead focuses on establishing the theoretical framework.

The implication of moderate or negligible attenuation in LRDs provides a resolution to the overestimation of AGN luminosities, and thus alleviates the tension in the classical Sołtan argument. Previous analyses by K. Inayoshi & K. Ichikawa (2024) require radiative efficiencies of $\gtrsim$20%–30% to reconcile the inferred BHAD with the BH mass density derived by assuming significant dust attenuation (J. E. Greene et al. 2024; V. Kokorev et al. 2024b; J. Matthee et al. 2024; H. B. Akins et al. 2025). In contrast, our model suggests that LRDs are consistent with a canonical 10% efficiency, aligning with the value inferred from normal AGN populations at lower redshifts over $0 < z < 5$.

Finally, our scenario predicts spectral evolution driven by binary orbital decay due to interactions with the circumbinary disk and GW emission, linking early-stage "proto-LRD" binaries to the broader AGN population and late-stage "LRD descendants" to coalescing binaries detectable by GW experiments using space-based interferometers (P. Amaro-Seoane et al. 2023; E.-K. Li et al. 2025a; H. Liu & K. Inayoshi 2025) and PTA setups (G. Agazie et al. 2023a, 2023b).

Acknowledgments

We greatly thank Kenta Hotokezaka and Hanpu Liu for constructive discussions. K.I., J.S., X.C., and L.C.H. acknowledge support from National Natural Science Foundation of China (grant Nos. 12573015, 1251101148, 12233001, and 12473037), the Beijing Natural Science Foundation (grant No. IS25003), and the China Manned Space Program (grant No. CMS-CSST-2025-A09). J.S. is also supported by "The Fundamental Research Funds for the Central Universities, Peking University" (grant No. 7100604896). Z.H. acknowledges support by US NSF grant AST-2006176 and by NASA grant Nos. 80NSSC24K0440 and 80NSSC22K0822.

Appendix A

Disk Energetics

Here, we describe the energy balance between the circumbinary disk and mini-disks, and provide the conditions for reproducing the V-shaped SED in this binary disk model.

In this model, the luminosity from the circumbinary disk is calculated as

$$L_{\rm cbd} = -\int_{2a}^{\infty} \frac{3GM\dot{M}}{2r^2} dr = \frac{\dot{M}_0 c^2}{20(1-p)}\left(\frac{a}{5R_{\rm S}}\right)^{p-1}, \tag{A1}$$

$$\simeq 0.071\,\dot{m}_0 L_{\rm Edd}\left(\frac{a}{10^3\,R_{\rm S}}\right)^{-1/2} \ {\rm for}\ p = 1/2. \tag{A2}$$

The mini-disks are responsible for the UV emission. The luminosity is estimated as

$$L_{{\rm md},i} = -\int_{r_{{\rm in},i}}^{r_{{\rm out},i}} \frac{3GM_i\dot{M}_i}{2r^2}\left(1 - \sqrt{\frac{r_{{\rm in},i}}{r}}\right) dr = \frac{1}{12} f_i \dot{M}_0 c^2, \tag{A3}$$

where we assume $r_{{\rm in},i} \ll r_{{\rm out},i}$, which is valid for most cases we consider in this paper, and where $a \sim 10^3\,R_{\rm S}$ and $q > 0.01$. Thus, the total mini-disk luminosity is $L_{\rm md} = L_{{\rm md},1} +$

$L_{\rm md,2} = (1/12)\dot{M}_0 c^2$. The luminosity density ratio between the far-UV (from the primary mini-disk) and optical (from the circumbinary disk) is given for $p = 1/2$ as

$$\frac{L_{\rm UV}}{L_{\rm opt}} \simeq \frac{L_{\rm md,1}}{L_{\rm cbd}} = \frac{5(1-p)f_1}{3}\left(\frac{a}{5R_{\rm S}}\right)^{1-p}, \tag{A4}$$

$$\simeq 1.2\left(\frac{f_1}{0.1}\right)\left(\frac{a}{10^3\,R_{\rm S}}\right)^{1/2}, \text{ for } p = 1/2. \tag{A5}$$

Keeping the turnover wavelength fixed at the Balmer limit, the ratio can be rewritten as

$$\frac{L_{\rm UV}}{L_{\rm opt}} \simeq 1.03\,\dot{m}_0^{1/5} M_7^{-1/5}\left(\frac{f_1}{0.1}\right)\left(\frac{\lambda_{\rm t}}{3646\ \text{Å}}\right)^{4/5}. \tag{A6}$$

Appendix B
Imprinting a Balmer Break on Transmitted Spectra

As discussed in K. Inayoshi & R. Maiolino (2025), dense gas surrounding an AGN can imprint a Balmer-break feature on the transmitted spectrum when the hydrogen number density of the gas slab is as high as $n_{\rm H} \simeq 10^{9-11}\,{\rm cm^{-3}}$, allowing atomic hydrogen to populate the $n = 2$ state. We compute the attenuated AGN spectra with nebular emission for hydrogen column densities of $N_{\rm H} = 10^{23}$ and $10^{24}\,{\rm cm^{-2}}$, assuming a hydrogen volume density of $n_{\rm H} = 10^{10}\,{\rm cm^{-3}}$, an ionization parameter of $\log U = -1.5$, and the incident AGN radiation spectrum as described in K. Inayoshi & R. Maiolino (2025). Here, we consider a dust-free gas slab to isolate the effects of pure gas absorption and reemission, and set a microturbulence velocity of $v_{\rm tur} = 100\,{\rm km\,s^{-1}}$ to smooth the Balmer break (e.g., X. Ji et al. 2025). The radiative transfer calculations are conducted with `CLOUDY` (G. J. Ferland et al. 2017).

To reproduce the overall continuum shape without resolving individual emission and absorption lines, we provide a simple analytical function for the transmission curve with six parameters of λ_0, λ_1, and s_i ($i = 1, 2, 3, 4$):

$$\mathcal{T}(\lambda) = \begin{cases} \exp\left[-\left(\frac{\lambda}{\lambda_0}\right)^{s_1} - \left(\frac{\lambda}{\lambda_1}\right)^{s_2}\right] & \text{for } \lambda < \lambda_{\rm B,lim}, \\ s_3 \cdot \tanh\left[s_4\left(\frac{\lambda}{\lambda_{\rm B,lim}} - 1\right)\right] & \text{for } \lambda \geqslant \lambda_{\rm B,lim}, \end{cases} \tag{B1}$$

where λ_0 and λ_1 characterize the continuum attenuation due to gas absorption at wavelengths redward of the Lyα line and blueward of the Balmer limit ($\lambda_{\rm B,lim} = 3646$ Å), respectively. The spectral shape redward of the Balmer limit is modeled using a hyperbolic tangent (tanh) function with a parameter s_4 controlling the smoothness of the break. This analytic expression offers a flexible description of the continuum shape modified by dense gas absorption, and is useful for fitting observed spectra in which the Balmer break is prominent. For the two cases of $N_{\rm H} = 10^{23}$ and $10^{24}\,{\rm cm^{-2}}$ with a covering fraction of 50%, the best-fit parameters are $(\lambda_0/\text{Å}, \lambda_1/\text{Å}, s_1, s_2, s_3, s_4) = (129$ $-26.00, 2.337, 0.9905, 34.70)$ and $(1499, 2140, -12.44, 1.847, 0.8707, 26.64)$, respectively.

Figure 8 shows the PRISM spectrum (gray line) and NIRCam and MIRI photometry (triangles) of MoM-BH*-1 (R. P. Naidu et al. 2025), which exhibits the strongest Balmer break among all spectroscopically observed LRDs. The spectral model includes a circumbinary disk and two mini-disks, computed for physical parameters of $M = 2 \times 10^7\,M_\odot$, $q = 0.1$, $\dot{m}_0 = 3$, $p = 0.75$, $a = 10^3\,R_{\rm S}$, and $A_V = 0.4$. The gas-attenuation transmission curve is adopted from Equation (B1) with $N_{\rm H} = 10^{24}\,{\rm cm^{-2}}$.

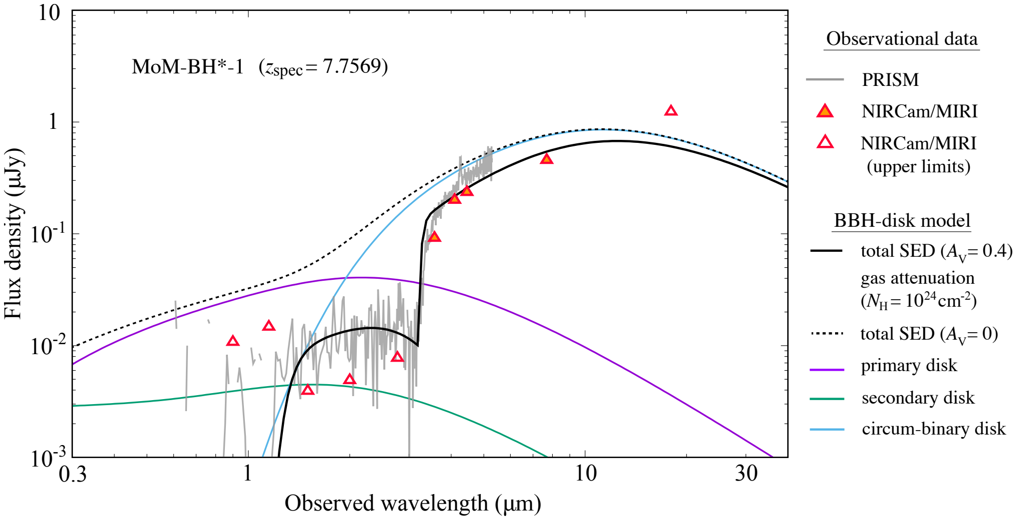

Figure 8. A spectral model for the LRD with the deepest Balmer break, MoM-BH*-1, at $z_{\rm spec} = 7.7569$, using NIRCam and MIRI photometry and PRISM spectra (R. P. Naidu et al. 2025). The binary BH-disk SED model assumes parameters $M = 2 \times 10^7\,M_\odot$, $q = 0.1$, $\dot{m}_0 = 3$, $p = 0.75$, $a = 10^3\,R_{\rm S}$, and $A_V = 0.4$. The gas-attenuation transmission curve is adopted from the fitting formula in Equation (B1) with $N_{\rm H} = 10^{24}\,{\rm cm^{-2}}$.

ORCID iDs

Kohei Inayoshi https://orcid.org/0000-0001-9840-4959
Jinyi Shangguan https://orcid.org/0000-0002-4569-9009
Xian Chen https://orcid.org/0000-0003-3950-9317
Luis C. Ho https://orcid.org/0000-0001-6947-5846
Zoltán Haiman https://orcid.org/0000-0003-3633-5403

References

Abramowicz, M. A., Czerny, B., Lasota, J. P., & Szuszkiewicz, E. 1988, ApJ, 332, 646
Abramowicz, M. A., Igumenshchev, I. V., Quataert, E., & Narayan, R. 2002, ApJ, 565, 1101
Agazie, G., Anumarlapudi, A., Archibald, A. M., et al. 2023a, ApJL, 951, L8
Agazie, G., Anumarlapudi, A., Archibald, A. M., et al. 2023b, ApJL, 952, L37
Akins, H. B., Casey, C. M., Lambrides, E., et al. 2025, ApJ, 991, 37
Amaro-Seoane, P., Andrews, J., Arca Sedda, M., et al. 2023, LRR, 26, 2
Anderson, M., Lehner, L., Megevand, M., & Neilsen, D. 2010, PhRvD, 81, 044004
Armitage, P. J., & Natarajan, P. 2002, ApJL, 567, L9
Artymowicz, P., & Lubow, S. H. 1994, ApJ, 421, 651
Bai, X.-N. 2011, ApJ, 739, 50
Balbus, S. A., & Hawley, J. F. 1998, RvMP, 70, 1
Barausse, E., Dvorkin, I., Tremmel, M., Volonteri, M., & Bonetti, M. 2020, ApJ, 904, 16
Barro, G., Pérez-González, P. G., Kocevski, D. D., et al. 2024, ApJ, 963, 128
Begelman, M. C., Rossi, E. M., & Armitage, P. J. 2008, MNRAS, 387, 1649
Begelman, M. C., Volonteri, M., & Rees, M. J. 2006, MNRAS, 370, 289
Blandford, R. D., & Znajek, R. L. 1977, MNRAS, 179, 433
Casey, C. M., Akins, H. B., Kokorev, V., et al. 2024, ApJL, 975, L4
Cerioli, A., Lodato, G., & Price, D. J. 2016, MNRAS, 457, 939
Chang, P., Strubbe, L. E., Menou, K., & Quataert, E. 2010, MNRAS, 407, 2007
Corrales, L. R., Haiman, Z., & MacFadyen, A. 2010, MNRAS, 404, 947
Coughlin, E. R., & Begelman, M. C. 2024, ApJ, 970, 158
Czerny, B., & Elvis, M. 1987, ApJ, 321, 305
de Graaff, A., Rix, H.-W., Naidu, R. P., et al. 2025, A&A, 701, A168
Delvecchio, I., Gruppioni, C., Pozzi, F., et al. 2014, MNRAS, 439, 2736
Dittmann, A. J., Ryan, G., & Miller, M. C. 2023, ApJL, 949, L30
Dong-Páez, C. A., Volonteri, M., Beckmann, R. S., et al. 2023, A&A, 676, A2
D'Orazio, D. J., & Duffell, P. C. 2021, ApJL, 914, L21
D'Orazio, D. J., Haiman, Z., Duffell, P., MacFadyen, A., & Farris, B. 2016, MNRAS, 459, 2379
D'Orazio, D. J., Haiman, Z., & MacFadyen, A. 2013, MNRAS, 436, 2997
D'Orazio, D. J., Haiman, Z., & Schiminovich, D. 2015, Natur, 525, 351
D'Orazio, D. J., & Samsing, J. 2018, MNRAS, 481, 4775
Duffell, P. C., D'Orazio, D., Derdzinski, A., et al. 2020, ApJ, 901, 25
Eggleton, P. P. 1983, ApJ, 268, 368
Ennoggi, L., Campanelli, M., Zlochower, Y., et al. 2025, PhRvD, 112, 063009
Enoki, M., & Nagashima, M. 2007, PThPh, 117, 241
Fakhouri, O., Ma, C.-P., & Boylan-Kolchin, M. 2010, MNRAS, 406, 2267
Farris, B. D., Duffell, P., MacFadyen, A. I., & Haiman, Z. 2014, ApJ, 783, 134
Farris, B. D., Duffell, P., MacFadyen, A. I., & Haiman, Z. 2015, MNRAS, 446, L36
Ferland, G. J., Chatzikos, M., Guzmán, F., et al. 2017, RMxAA, 53, 385
Fontecilla, C., Chen, X., & Cuadra, J. 2017, MNRAS, 468, L50
Furtak, L. J., Secunda, A. R., Greene, J. E., et al. 2025, A&A, 698, A227
Furtak, L. J., Zitrin, A., Plat, A., et al. 2023, ApJ, 952, 142
Gloudemans, A. J., Duncan, K. J., Eilers, A.-C., et al. 2025, ApJ, 986, 130
Greene, J. E., Labbe, I., Goulding, A. D., et al. 2024, ApJ, 964, 39
Haiman, Z., Kocsis, B., & Menou, K. 2009, ApJ, 700, 1952
Hainline, K. N., Maiolino, R., Juodžbalis, I., et al. 2025, ApJ, 979, 138
Harikane, Y., Zhang, Y., Nakajima, K., et al. 2023, ApJ, 959, 39
Hayashi, C. 1961, PASJ, 13, 450
Ho, L. C. 1999, ApJ, 516, 672
Ho, L. C. 2002, ApJ, 564, 120
Ho, L. C. 2008, ARA&A, 46, 475
Hoshi, R. 1979, PThPh, 61, 1307
Hosokawa, T., Yorke, H. W., Inayoshi, K., Omukai, K., & Yoshida, N. 2013, ApJ, 778, 178
Hu, H., Inayoshi, K., Haiman, Z., Quataert, E., & Kuiper, R. 2022, ApJ, 934, 132
Inayoshi, K. 2025, ApJL, 988, L22
Inayoshi, K., Haiman, Z., & Ostriker, J. P. 2016, MNRAS, 459, 3738
Inayoshi, K., & Ichikawa, K. 2024, ApJL, 973, L49
Inayoshi, K., Ichikawa, K., & Haiman, Z. 2018, ApJL, 863, L36
Inayoshi, K., Kimura, S. S., & Noda, H. 2025, PASJ, 77, 811
Inayoshi, K., & Maiolino, R. 2025, ApJL, 980, L27
Ivezić, Ž., Kahn, S. M., Tyson, J. A., et al. 2019, ApJ, 873, 111
Ji, X., Maiolino, R., Übler, H., et al. 2025, MNRAS, 544, 3900
Jiang, L., McGreer, I. D., Fan, X., et al. 2016, ApJ, 833, 222
Jiang, Y.-F., Stone, J. M., & Davis, S. W. 2014, ApJ, 796, 106
Kato, S., Fukue, J., & Mineshige, S. 2008, Black-Hole Accretion Disks: Towards a New Paradigm (Kyoto Univ. Press)
Kelley, L. Z., Blecha, L., Hernquist, L., Sesana, A., & Taylor, S. R. 2017, MNRAS, 471, 4508
Kelley, L. Z., Haiman, Z., Sesana, A., & Hernquist, L. 2019, MNRAS, 485, 1579
Khan, F. M., Davis, B. L., Macciò, A. V., & Holley-Bockelmann, K. 2025, ApJL, 986, L1
Kido, D., Ioka, K., Hotokezaka, K., Inayoshi, K., & Irwin, C. M. 2025, MNRAS, 544, 3407
Kis-Tóth, Á., Haiman, Z., & Frei, Z. 2025, CQGra, 42, 075007
Kocevski, D. D., Finkelstein, S. L., Barro, G., et al. 2025, ApJ, 986, 126
Kocevski, D. D., Onoue, M., Inayoshi, K., et al. 2023, ApJL, 954, L4
Kokorev, V., Caputi, K. I., Greene, J. E., et al. 2024a, ApJ, 968, 38
Kokorev, V., Chisholm, J., Endsley, R., et al. 2024b, ApJ, 975, 178
Kokubo, M., & Harikane, Y. 2025, ApJ, 995, 24
Krauth, L. M., Davelaar, J., Haiman, Z., et al. 2023, MNRAS, 526, 5441
Labbe, I., Greene, J. E., Matthee, J., et al. 2024, arXiv:2412.04557
Labbe, I., Greene, J. E., Bezanson, R., et al. 2025, ApJ, 978, 92
Lai, D., & Muñoz, D. J. 2023, ARA&A, 61, 517
Lambrides, E., Garofali, K., Larson, R., et al. 2024, arXiv:2409.13047
Laor, A., & Draine, B. T. 1993, ApJ, 402, 441
Laor, A., & Netzer, H. 1989, MNRAS, 238, 897
Li, E.-K., Liu, S., Torres-Orjuela, A., et al. 2025a, RPPh, 88, 056901
Li, Z., Inayoshi, K., Chen, K., Ichikawa, K., & Ho, L. C. 2025b, ApJ, 980, 36
Lin, D. N. C., & Papaloizou, J. 1979, MNRAS, 186, 799
Lin, D. N. C., & Papaloizou, J. 1986, ApJ, 309, 846
Lin, X., Fan, X., Wang, F., et al. 2026, ApJ, 996, 93
Lin, X., Wang, F., Fan, X., et al. 2024, ApJ, 974, 147
Lippai, Z., Frei, Z., & Haiman, Z. 2008, ApJL, 676, L5
Liu, H., & Inayoshi, K. 2025, PhRvD, 111, 043012
Lodato, G., Nayakshin, S., King, A. R., & Pringle, J. E. 2009, MNRAS, 398, 1392
Ma, Y., Greene, J. E., Setton, D. J., et al. 2025, ApJ, 981, 191
MacFadyen, A. I., & Milosavljević, M. 2008, ApJ, 672, 83
Madau, P., & Haardt, F. 2024, ApJL, 976, L24
Mahesh, S., McWilliams, S. T., & Pirog, M. 2024, ApJ, 973, 18
Maiolino, R., Risaliti, G., Signorini, M., et al. 2025, MNRAS, 538, 1921
Maiolino, R., Scholtz, J., Curtis-Lake, E., et al. 2024, A&A, 691, A145
Matsuoka, Y., Onoue, M., Kashikawa, N., et al. 2016, ApJ, 828, 26
Matsuoka, Y., Onoue, M., Iwasawa, K., et al. 2023, ApJL, 949, L42
Matthee, J., Naidu, R. P., Brammer, G., et al. 2024, ApJ, 963, 129
Mayer, L., Capelo, P. R., Zwick, L., & Di Matteo, T. 2024, ApJ, 961, 76
Mazzolari, G., Gilli, R., Maiolino, R., et al. 2026, A&A, 706, A372
McKernan, B., Ford, K. E. S., Kocsis, B., & Haiman, Z. 2013, MNRAS, 432, 1468
Megevand, M., Anderson, M., Frank, J., et al. 2009, PhRvD, 80, 024012
Meyer, F., & Meyer-Hofmeister, E. 1982, A&A, 106, 34
Mineshige, S., & Osaki, Y. 1983, PASJ, 35, 377
Miranda, R., Muñoz, D. J., & Lai, D. 2017, MNRAS, 466, 1170
Muñoz, D. J., & Lai, D. 2016, ApJ, 827, 43
Muñoz, D. J., Lai, D., Kratter, K., & Miranda, R. 2020, ApJ, 889, 114
Muñoz, D. J., Miranda, R., & Lai, D. 2019, ApJ, 871, 84
Naidu, R. P., Matthee, J., Katz, H., et al. 2025, arXiv:2503.16596
Niida, M., Nagao, T., Ikeda, H., et al. 2020, ApJ, 904, 89
Ohsuga, K., Mori, M., Nakamoto, T., & Mineshige, S. 2005, ApJ, 628, 368
O'Neill, D., Tiede, C., D'Orazio, D. J., Haiman, Z., & MacFadyen, A. 2025, ApJ, 993, 206
Pacucci, F., & Narayan, R. 2024, ApJ, 976, 96
Pérez-González, P. G., Barro, G., Rieke, G. H., et al. 2024, ApJ, 968, 4
Peters, P. C., & Mathews, J. 1963, PhRv, 131, 435
Phinney, E. S. 2001, arXiv:astro-ph/0108028
Ricarte, A., & Natarajan, P. 2018, MNRAS, 481, 3278
Roedig, C., Krolik, J. H., & Miller, M. C. 2014, ApJ, 785, 115
Rossi, E. M., Lodato, G., Armitage, P. J., Pringle, J. E., & King, A. R. 2010, MNRAS, 401, 2021
Rudak, B., & Paczynski, B. 1981, AcA, 31, 13
Rusakov, V., Watson, D., Nikopoulos, G. P., et al. 2026, Natur, 649, 574

Saade, M. L., Brightman, M., Stern, D., et al. 2024, ApJ, 966, 104
Saade, M. L., Stern, D., Brightman, M., et al. 2020, ApJ, 900, 148
Sądowski, A., Narayan, R., Tchekhovskoy, A., et al. 2015, MNRAS, 447, 49
Schnittman, J. D., & Krolik, J. H. 2008, ApJ, 684, 835
Scholtz, J., Maiolino, R., D'Eugenio, F., et al. 2025, A&A, 697, A175
Sesana, A. 2013, CQGra, 30, 224014
Setton, D. J., Greene, J. E., de Graaff, A., et al. 2025a, ApJ, 995, 118
Setton, D. J., Greene, J. E., Spilker, J. S., et al. 2025b, ApJL, 991, L10
Shakura, N. I., & Sunyaev, R. A. 1973, A&A, 24, 337
Shi, Y., Kremer, K., Grudić, M. Y., Gerling-Dunsmore, H. J., & Hopkins, P. F. 2023, MNRAS, 518, 3606
Siwek, M., Weinberger, R., & Hernquist, L. 2023, MNRAS, 522, 2707
Soltan, A. 1982, MNRAS, 200, 115
Spergel, D., Gehrels, N., Baltay, C., et al. 2015, arXiv:1503.03757
Stone, J. M., & Pringle, J. E. 2001, MNRAS, 322, 461
Takeo, E., Inayoshi, K., & Mineshige, S. 2020, MNRAS, 497, 302
Tang, Y., Haiman, Z., & MacFadyen, A. 2018, MNRAS, 476, 2249
Taylor, A. J., Finkelstein, S. L., Kocevski, D. D., et al. 2025a, ApJ, 986, 165
Taylor, A. J., Kokorev, V., Kocevski, D. D., et al. 2025b, ApJL, 989, L7
Tiede, C., Zrake, J., MacFadyen, A., & Haiman, Z. 2025, ApJ, 984, 144
Ueda, Y., Akiyama, M., Hasinger, G., Miyaji, T., & Watson, M. G. 2014, ApJ, 786, 104
Vanden Berk, D. E., Richards, G. T., Bauer, A., et al. 2001, AJ, 122, 549
Veilleux, S., Kim, D. C., & Sanders, D. B. 2002, ApJS, 143, 315
Volonteri, M., & Begelman, M. C. 2010, MNRAS, 409, 1022
Volonteri, M., Pfister, H., Beckmann, R. S., et al. 2020, MNRAS, 498, 2219
Wang, B., de Graaff, A., Davies, R. L., et al. 2025, ApJ, 984, 121
Wang, B., Leja, J., de Graaff, A., et al. 2024, ApJL, 969, L13
Watarai, K.-y. 2006, ApJ, 648, 523
Westernacher-Schneider, J. R., Zrake, J., MacFadyen, A., & Haiman, Z. 2022, PhRvD, 106, 103010
Williams, C. C., Alberts, S., Ji, Z., et al. 2024, ApJ, 968, 34
Woods, T. E., Patrick, S., Elford, J. S., Whalen, D. J., & Heger, A. 2021, ApJ, 915, 110
Xin, C., & Haiman, Z. 2021, MNRAS, 506, 2408
Xin, C., & Haiman, Z. 2024, MNRAS, 533, 3164
Yan, C.-S., Lu, Y., Yu, Q., Mao, S., & Wambsganss, J. 2014, ApJ, 784, 100
Yu, Q., & Tremaine, S. 2002, MNRAS, 335, 965
Yuan, F., & Narayan, R. 2014, ARA&A, 52, 529
Yue, M., Eilers, A.-C., Ananna, T. T., et al. 2024, ApJL, 974, L26
Zhang, Z., Jiang, L., Liu, W., & Ho, L. C. 2025, ApJ, 985, 119
Zrake, J., Tiede, C., MacFadyen, A., & Haiman, Z. 2021, ApJL, 909, L13